Acta Oceanol. Sin., 2024, Vol. 43, No. 7, P. 1–14
https://doi.org/10.1007/s13131-023-2228-0
http://www.aosocean.com
E-mail: ocean2@hyxb.org.cn

Responses of the Southern Ocean mixed layer depth to the eastern and central Pacific El Niño events during austral winter

Yuxin Shi[1], Hailong Liu[2]*, Xidong Wang[3], Quanan Zheng[4]

[1] School of Oceanography, Shanghai Jiao Tong University, Shanghai 200240, China

[2] Yunnan Key Laboratory of Meteorological Disasters and Climate Resources in the Greater Mekong Subregion, Yunnan University, Kunming 600650, China

[3] College of Oceanography, Hohai University, Nanjing 210098, China

[4] Department of Atmospheric and Oceanic Science, University of Maryland at College Park, College Park 20742, USA

Received 8 February 2023; accepted 26 May 2023

Abstract

Based on the Ocean Reanalysis System version 5 (ORAS5) and the fifth-generation reanalysis datasets derived from European Centre for Medium-Range Weather Forecasts (ERA5), we investigate the different impacts of the central Pacific (CP) El Niño and the eastern Pacific (EP) El Niño on the Southern Ocean (SO) mixed layer depth (MLD) during austral winter. The MLD response to the EP El Niño shows a dipole pattern in the South Pacific, namely the MLD dipole, which is the leading El Niño-induced MLD variability in the SO. The tropical Pacific warm sea surface temperature anomaly (SSTA) signal associated with the EP El Niño excites a Rossby wave train propagating southeastward and then enhances the Amundsen Sea low (ASL). This results in an anomalous cyclone over the Amundsen Sea. As a result, the anomalous southerly wind to the west of this anomalous cyclone advects colder and drier air into the southeast of New Zealand, leading to surface cooling through less total surface heat flux, especially surface sensible heat (SH) flux and latent heat (LH) flux, and thus contributing to the mix layer (ML) deepening. The east of the anomalous cyclone brings warmer and wetter air to the southwest of Chile, but the total heat flux anomaly shows no significant change. The warm air promotes the sea ice melting and maintains fresh water, which strengthens stratification. This results in a shallower MLD. During the CP El Niño, the response of MLD shows a separate negative MLD anomaly center in the central South Pacific. The Rossby wave train triggered by the warm SSTA in the central Pacific Ocean spreads to the Amundsen Sea, which weakens the ASL. Therefore, the anomalous anticyclone dominates the Amundsen Sea. Consequently, the anomalous northerly wind to the west of anomalous anticyclone advects warmer and wetter air into the central and southern Pacific, causing surface warming through increased SH, LH, and longwave radiation flux, and thus contributing to the ML shoaling. However, to the east of the anomalous anticyclone, there is no statistically significant impact on the MLD.

Key words: Southern Ocean, mixed layer depth, Central Pacific El Niño, Eastern Pacific El Niño, Rossby wave train

Citation: Shi Yuxin, Liu Hailong, Wang Xidong, Zheng Quanan. 2024. Responses of the Southern Ocean mixed layer depth to the eastern and central Pacific El Niño events during austral winter. Acta Oceanologica Sinica, 43(7): 1–14, doi: 10.1007/s13131-023-2228-0

1 Introduction

The Southern Ocean (SO, 30°–85°S, 0°E–180°–0°W) is an important field for the global Meridional Overturning Circulation (MOC) and deep ocean water formation (Kuhlbrodt et al., 2007). The SO is also a key region for the global carbon cycle, air-sea exchange and heat redistribution (Arrigo et al., 2008; Park et al., 2010; Sarmiento et al., 1998). The mixed layer (ML) refers to a near ocean surface water layer with an almost vertical uniformity of temperature, salinity, density and other physical properties, resulting from the wind mixing and effects of ocean internal processes (Carton et al., 2008; Holte and Talley, 2009; Liu et al., 2009). As a bridge between the atmosphere and the ocean, the properties and dynamical processes in the ML have significant effects on the exchange of mass, heat and momentum between air and sea (Kara et al., 2003; de Boyer Montégut et al., 2007). Thus, the mixed layer depth (MLD) in the SO plays a crucial role in global climate regulation. On the other hand, there is a large amount of phytoplankton living in the ML. The variability of MLD has great influences on the availability of light and nutrients, modulating the heat and nutrient exchange between the well-lit surface layer and the dark deep layer, which dominates the growth and distribution of phytoplankton (Mitchell et al., 1991; Sallée et al., 2010). Besides, changes in phytoplankton can further affect primary productivity and even ecosystems through food webs, especially in the SO where the krill is abundant. Dynamic processes of ML in the SO can thus alter the ocean capacity of storing heat and carbon, as well as the availability of light and nutrients for phytoplankton growth. Above all, the SO ML has a pivotal impact on global climate change and ecosystems due to its unique characteristics. Therefore, it is important to study the variability of MLD in the SO, particularly the links with the dominant mode of atmospheric and oceanic variabilities.

Numerous studies in the literature have linked the variability of the SO MLD to sea ice, Amundsen Sea low (ASL), El Niño-

Foundation item: The Oceanic Interdisciplinary Program of Shanghai Jiao Tong University under contract No. SL2021ZD204; the Sino-German Mobility Program under contract No. M0333; the grant of Shanghai Frontiers Science Center of Polar Science (SCOPS).
*Corresponding author, E-mail: hailong.liu@ynu.edu.cn

Southern Oscillation (ENSO) and the Southern Annular Mode (SAM) through observations and models on various time scales (Gupta and England, 2006; Li et al., 2019; Nardelli et al., 2017; Sallée et al., 2010; Vivier et al., 2010). However, the SO MLD responds most significantly to the SAM and the ENSO, and the influences of the SAM and the ENSO are dominant on the interannual time scale (Li and England, 2020; Sallée et al., 2010). Meanwhile, the response of the SO MLD to the SAM shows a wave-3 pattern in the latitudinal band between 35°S and 55°S, with the maximum anomaly close to New Zealand, south-west of Australia and the east of Chile. The wave-3 pattern is caused by the combined effects of net heat flux and meridional wind (Sallée et al., 2010; Zhang et al., 2018). In addition, the sea surface temperature anomaly (SSTA) in the South Pacific also exhibits a similar tripole-like structure, suggesting that the MLD variability has an impact on SST (Li et al., 2014b).

As for ENSO, although it occurs in the tropics, previous studies have shown that its effects extend to extratropical variations of the southern hemisphere and even high-latitude regions covered by sea ice (Ciasto and England, 2011; Schneider et al., 2012; Turner, 2004). Meanwhile, previous studies have revealed the mechanisms of ENSO-induced anomalies of specific climate variables in the southern hemisphere, such as surface air temperature, sea surface temperature (SST), sea ice concentration, and MLD (Ciasto and England, 2011; Ding et al., 2011; Li and England, 2020). The impact of ENSO on the SO MLD is mainly concentrated in the Pacific sector. Using the model data, Li and England (2020) found that the anomalous ASL intensification associated with the ENSO affects the variation of the MLD in the Pacific sector during the austral winter (June, July, and August; JJA). In turn, the MLD response is characterized by a dipole pattern with a positive MLD anomaly center in the central Pacific (surrounding 120°W) and a negative MLD anomaly center in the southwest Pacific (surrounding New Zealand). This is closely related to the airflow around the anomalous sea level pressure (SLP) center in the Amundsen Sea.

The ENSO can modulate the austral winter MLD in the South Pacific via the teleconnection between it and the ASL (Li and England, 2020). The teleconnection is realized by the Rossby wave train propagation emanating from the equatorial Pacific Ocean into the Antarctic (Hoskins and Karoly, 1981; Turner, 2004), which is known as the Pacific-South American (PSA) teleconnection pattern (Kidson, 1999; Mo and Ghil, 1987; Mo and Higgins, 1998). Positive SSTA in the tropical Pacific related to the positive phase ENSO can be regarded as an effective Rossby wave source, which excites the stationary Rossby wave train in the upper troposphere (Cai et al., 2011; Clem and Fogt, 2015; Fogt et al., 2011; L'Heureux and Thompson, 2006), which propagates poleward, with the alternating occurrence of high pressure anomaly centers and lowpressure anomaly centers, eventually reaching ASL and interacting with the ASL (Li et al., 2021; Meehl et al., 2016; Zhang et al., 2021). The ASL, in turn, is abnormally deepened. As a consequence, colder southerly wind anomaly and warmer northerly wind anomaly appear to the west and east of the anomalous cyclone respectively, thus contributing to the dipole distribution of MLD in the South Pacific (Li and England, 2020).

Moreover, growing number of studies suggest that tropical-polar teleconnections can also originate from other tropical oceans except for the Pacific Ocean (Cai et al., 2019; Li et al., 2014a, 2015a; Nuncio and Yuan, 2015). They affect the SO on different time scales, either through individual or combined impact (Li and England, 2020; Meehl et al., 2016; Rondanelli et al., 2019; Zhang et al., 2021). In addition to the ENSO, signals from the tropical Indian Ocean, especially the Indian Ocean Dipole (IOD), also play an instrumental role in the generation and propagation of the Rossby wave train (Cai et al., 2014; Luo et al., 2010; Saji et al., 2005). When these two major tropical climate variabilities coexist, such as El Niño accompanied by a positive phase IOD, the Rossby wave train can reach farther to the Bellingshausen Sea. Therefore, they can work together to influence the SO MLD (Cai et al., 2011; Li and England, 2020; Zhang et al., 2021).

The aforementioned studies reveal that the tropical diabatic heating caused by the El Niño can act as the effective Rossby wave source, and trigger a southeastward propagating Rossby wave train in the upper troposphere, thus affecting the SO MLD (Hoskins and Karoly, 1981; Karoly and Hoskins, 1983; Li and England, 2020; Turner, 2004). The different categorization of El Niño was used by previous investigators. For example, Yu and Kao (2007) categorized the El Niño events into two types based on the location of maximum SSTA, namely, the central Pacific (CP) El Niño with maximum SSTA occurring in the central tropical Pacific and the eastern Pacific (EP) El Niño with maximum SSTA in the eastern tropical Pacific (Kao and Yu, 2009; Yu and Kao, 2007). Similarly, Kug et al. (2009) categorized the El Niño events into cold tongue (CT) El Niño and warm pool (WP) El Niño based on the spatial distribution of SSTA. The CT El Niño is typically known as the conventional El Niño, which is distinguished by the presence of considerable SSTA in the Niño 3 region (between 5°S and 5°N and 150°W to 90°W). In contrast, the WP El Niño is characterized by the occurrence of SSTA that are mostly restricted to the Niño 4 region (between 5°S and 5°N and 160°E to 150°W).

This study follows the definitions by Yu and Kao (2007). Using reanalysis data, Wang et al. (2020) examined the effects of EP and CP El Niño events on the SO MLD from 1979 to 1998. They found that the response of the MLD to CP and EP El Niño is relatively strong in austral winter and spring. The MLD response exhibits a seesaw pattern, located on the flanks of South America. The positive MLD anomaly center of the seesaw arises in the Southwest Atlantic and the negative anomaly center occurs in the Southeast Pacific. This feature could be found in two types of El Niño events in spring, and it is mainly controlled by sea surface heat flux anomaly. However, the seesaw pattern disappears during the austral winter for both EP and CP El Niño events. Two types of El Niño events are quite distinct in terms of generation and development mechanisms (Chen et al., 2019), so that have different impacts on the SO MLD. However, previous studies focused mainly on the impacts of classified El Niño events on the SO MLD (Wang et al., 2020). It has not been well understood what are the distinct effects and mechanisms of EP and CP El Niño events on the variation of SO MLD. Compared with the unclassified El Niño event, the impacts of EP and CP El Niño events on the SO MLD are more complex. Thus, this study aims to explore the different responses of the SO MLD to two-type El Niño events during austral winter when the influence of EP and CP El Niño events on the SO MLD is greatest (Li and England, 2020).

The remainder of this paper is organized as follows. Section 2 briefly describes the datasets and methods used in this paper. Next, MLD variabilities induced by EP and CP El Niño events are presented respectively in Section 3. Section 4 investigates the different characteristics of tropical-polar teleconnections during the EP and CP El Niño events. Section 5 further illustrates possible modulation mechanisms of MLD variability during the EP and CP El Niño events. Discussion and conclusions are given in Section 6.

2 Data and methods

2.1 *Datasets*

This study uses the monthly data derived from the European Centre for Medium-Range Weather Forecasts (ECMWF) Ocean Reanalysis System version 5 (ORAS5) from January 1980 to December 2021 as a baseline (Zuo et al., 2019). The horizontal resolution is 0.25° × 0.25° with 75 layers in the vertical direction. Variables include potential temperature, salinity, and sea ice concentration (SIC), where potential temperature and salinity are used to estimate the MLD in the SO. Another primary dataset for this study is the fifth-generation ECMWF reanalysis data (ERA5; Bell et al., 2021; Hersbach et al., 2020). The ERA5 has a horizontal resolution of 0.25° × 0.25° and covers the period from January 1980 to December 2021. Geopotential height from 300 hPa, 700 hPa, and 850 hPa, SLP, horizontal wind fields at 300 hPa and 10 m, air temperature at 2 m, surface specific humidity (1 000 hPa), SST, surface sensible heat flux (SH), latent heat flux (LH), net longwave radiation flux (LW), shortwave radiation flux (SW), and potential vorticity (PV) obtained from ERA5 are the basis for mechanism analysis. Besides, monthly Niño 3 and Niño 4 indices based on the Hadley Centre Global Sea Ice and Sea Surface Temperature (HadISST), spanning from January 1980 to December 2021, are derived from the National Oceanic and Atmospheric Administration (NOAA) Physical Sciences Laboratory (PSL) (Rayner et al., 2003).

2.2 *MLD estimation*

In this study, the MLD is defined as the minimum depth of temperature-criteria mixed layer (ML_t), salinity-criteria mixed layer (ML_s) and density-criteria mixed layer (ML_d) (Helber et al., 2012). To unify the criteria for calculating the MLD for each variable so that the calculation results can be compared, 0.2℃ (ΔT) is selected as a threshold value, and 10 m is used as the reference layer (Dong et al., 2008; Duan et al., 2012; de Boyer Montégut et al., 2004; Xiao et al., 2013). By taking the reference layer at 10 m, the influence of abnormal thermal processes on the ocean surface, such as freshwater input and rapid evaporation, can be removed. The threshold of 0.2℃ is the optimal temperature threshold and considered as the most appropriate estimation from individual profiles, which has been used broadly in previous studies (Bosc et al., 2009; Dong et al., 2007, 2008; Foltz and McPhaden, 2009; Liu et al., 2009; Ying et al., 2019). Therefore, 0.2℃ is the temperature threshold (ΔT) for calculating the ML_t. The density threshold ($\Delta\theta$) used to calculate ML_d is the density increase corresponding to a 0.2℃ temperature decrease compared to the reference layer when the salinity is constant. Similarly, the threshold (ΔS) of ML_s is the salinity increase associated with a density increase ($\Delta\theta_s$) compared to the reference layer when the temperature is constant. To make a valid comparison and then find the shallowest one of the three (ML_t, ML_s, and ML_d), $\Delta\theta$ and $\Delta\theta_s$ should be equal. Therefore, the salinity threshold ΔS is calculated by increasing the salinity by 0.01 increments until the $\Delta\theta_s$ is equal or exceeded (Helber et al., 2012). These are presented as follows:

$$\Delta\theta = \theta\left(T_{10} - \Delta T, S_{10}, P_0\right) - \theta\left(T_{10}, S_{10}, P_0\right), \tag{1}$$

$$\Delta S = 0.01n,\ \ n = 1, 2, ..., N_{\mathrm{mld}}, \tag{2}$$

$$\Delta\theta_s = \theta\left(T_{10}, S_{10} + \Delta S, P_0\right) - \theta\left(T_{10}, S_{10}, P_0\right), \tag{3}$$

$$\Delta\theta_s = \Delta\theta, \tag{4}$$

where T_{10} and S_{10} are the potential temperature and salinity at the reference depth of 10 m, P_0 is the pressure at the ocean surface, which the depth is 0 m. ΔT is equal to 0.2℃ as mentioned above.

2.3 *Two Niño indices*

We use N_{ep} and N_{cp} to categorize the EP and CP El Niño events according to Ren and Jin (2011). These are presented as

$$\begin{cases} N_{ep} = N_3 - \alpha N_4, \\ N_{cp} = N_4 - \alpha N_3, \end{cases} \tag{5}$$

$$\alpha = \begin{cases} 2/5, & N_3 N_4 > 0, \\ 0, & \text{otherwise}, \end{cases} \tag{6}$$

and N_3 and N_4 are the Niño 3 and Niño 4 indices, respectively. The indices are averaged monthly SSTA in the Niño 3 region (5°N–5°S, 150°–90°W) and Niño 4 region (5°N–5°S, 160°E–180°–150°W), respectively.

3 Observed MLD variability during EP and CP El Niño events

Before considering the MLD changes caused by two types of El Niño events, it is first important to consider which El Niño years belong to the EP and CP El Niño events. According to previous studies, Niño 3 and Niño 4 indices can be adequately used to represent EP and CP El Niño events (Kug et al., 2009; Yeh et al., 2009). However, Ren and Jin (2011) further proposed two new El Niño indices based on Niño 3 and Niño 4 indices (see Eq. (5)). Figure 1 shows the time evolution of Niño 3 and Niño 4 indices (blue lines) and two new El Niño indices named N_{ep} and N_{cp} (red lines). Consider that El Niño events typically reach peaks during boreal winter (December, January, and February; DJF) (Zhang et al., 2019), only boreal winter years with indices larger than one standard deviation are selected for this study to avoid interfering with subsequent composite results. One can see that Niño 3 and N_{ep} are highly correlated (Fig. 1a, r = 0.95). The difference between the two is generally minor, especially in years with the strongest EP El Niño, such as 1982/1983 and 1997/1998. It indicates that both Niño 3 and N_{ep} indices can capture EP El Niño events well. Although Niño 4 index is also highly correlated with the N_{cp} index (Fig. 1b, r = 0.82), the difference between Niño 4 and N_{cp} indices is more pronounced compared to the difference between Niño 3 and N_{ep} (Fig. 1a). Specifically, during the periods of the strongest El Niño events, Niño 4 and N_{cp} indices are almost out of phase, such as 1982/1983, 1997/1998, and 2015/2016.

In general, fluctuation amplitudes of N_{ep} and N_{cp} indices tend to be a little smaller than that of Niño 3 and Niño 4 indices. That is, some years may be classified as the EP El Niño or the CP El Niño events if classified according to Niño 3 and Niño 4 indices, but may not be when classified by N_{cp} and N_{ep}. In addition, when the CP El Niño events occur, N_{ep} becomes less than one standard deviation in most cases, while the Niño 3 indices are still larger than one standard deviation, such as 1994/1995, 2014/2015, and 2018/2019. This indicates that N_{cp} and N_{ep} indices are relatively independent, while Niño 3 and Niño 4 indices are interrelated. According to these characteristics, N_{cp} and N_{ep} indices thus are used as the basis for dividing two types of El Niño events. Ultimately, as listed in Table 1, five EP El Niño and eight CP El Niño events are selected during 1980–2021. It is worth noting that both N_{cp} and N_{ep} indices exceeded one standard deviation during

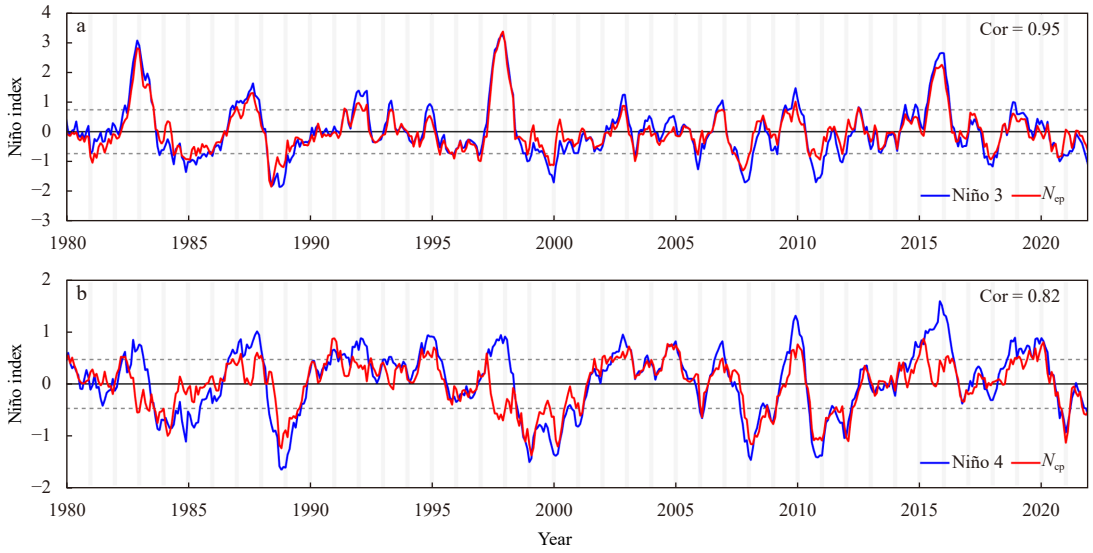

Fig. 1. Time series of Niño 3 index (blue line) from NOAA and N_{ep} index (red line) based on Eq. (5) (a), and Niño 4 index (blue line) from NOAA and N_{cp} index (red line) based on Eq. (5) (b). Grey dashed lines denote one standard deviation of N_{ep} and N_{cp} indices. Cor indicates correlations between two curves in each panel.

Table 1. Category of EP El Niño and CP El Niño events from 1980 to 2021 determined by N_{ep} and N_{cp} indices

Category	Year
EP El Niño	1982/1983, 1991/1992, 1997/1998, 2006/2007, 2015/2016
CP El Niño	1990/1991, 1994/1995, 2002/2003, 2004/2005, 2009/2010, 2014/2015, 2018/2019, 2019/2020

1987/1988, so it was classified as mixed type, starting with the EP El Niño and subsequently shifting into the CP El Niño (Wang et al., 2018a). Comparing with the previous finding using the same N_{ep} and N_{cp} indices, the selection of EP El Niño years is identical. However, the selection of CP El Niño years is different. This study has two more CP Niño years, namely 1990/1991 and 2019/2020. This difference may be attributed to different SST data used to calculate N_3 and N_4 in Eq. (2), as well as different study periods. The analysis period for the previous study was from 1980 to 2019, while that for this study from 1980 to 2021 (Zhang et al., 2021). In addition, the comparison is made to the conventional definition of two-types of El Niño. The years of EP and CP El Niño are robust over the same research period, except for the mixed type of El Niño event (such as 1987/1988) (Wang et al., 2017; Zhang et al., 2011).

Figure 2 shows composite images of seasonal mean MLD an-

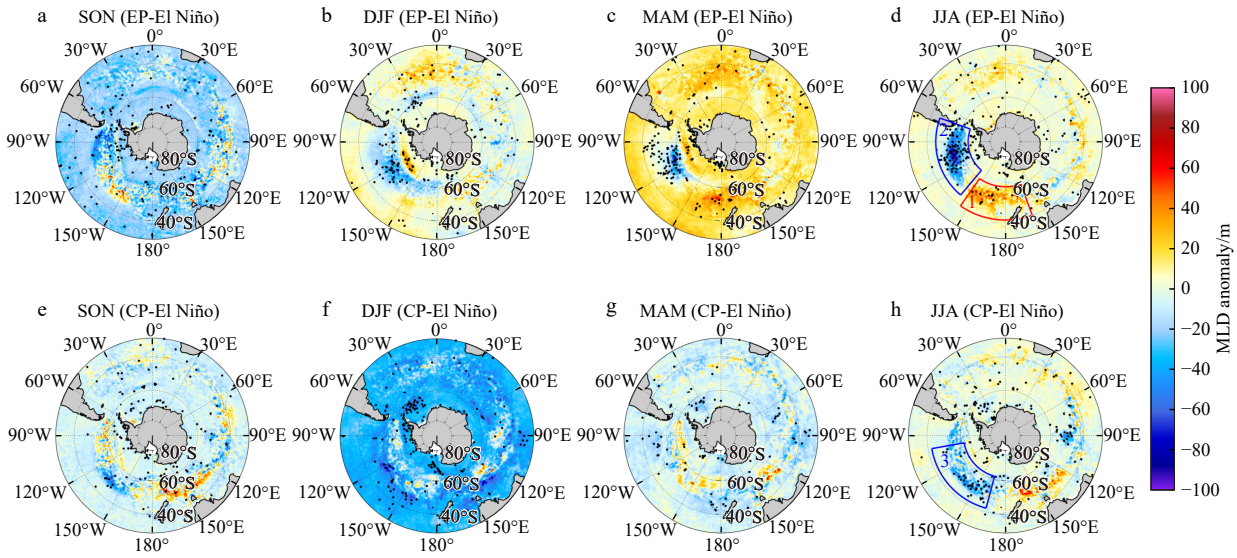

Fig. 2. Composite images of MLD anomaly derived from the ORAS5 in austral, spring (SON) (a, e), summer (DJF) (b, f), autumn (MAM) (c, g), and winter (JJA) (d, h) for EP El Niño (a–d) and CP El Niño (e–h) events. The black stippled areas represent that the results are statistically significant at the 95% confidence level. Box 1 (red; 40°–60°S, 160°E–180°–145°W) and Box 2 (blue; 45°–65°S, 140°–70°W) in d and the Box 3 (blue; 42°–62°S, 165°–100°W) in h indicate the focus areas. SON: September, October, and November; DJF: December, January, and February; MAM: March, April, and May; JJA: June, July, and August.

omaly in the SO for five EP and eight CP El Niño events listed in Table 1. Overall, the MLD anomaly in the Pacific sector is evident in both EP and CP El Niño events throughout the year, while the MLD anomaly in the Atlantic and Indian Ocean sectors is weaker. The notable anomalous regions are mainly concentrated in the high latitude region between 40°S and 70°S. In austral spring (September, October, and November; SON) during EP El Niño events, the distribution of MLD anomaly shows a dipole pattern in the Pacific sector, with the positive and negative anomaly centers in the central and eastern Pacific, respectively (Fig. 2a). The other sectors have no obvious distribution features. Although the spatial structure is obvious, the MLD anomaly is not statistically significant at the 95% confidence level. For the austral spring of CP-El Niño, the distributions of MLD anomaly in the SO bear a resemblance to that of EP El Niño events, except that the phases are opposite. Furthermore, only weak and statistically significant negative MLD anomaly occurs in the central Pacific Ocean (Fig. 2e). During the subsequent austral summer (DJF) and autumn (March, April, May; MAM), the distribution characteristics of MLD anomaly in the SO are similar to that during the EP El Niño, with weak and statistically significant negative anomaly centers in the central Pacific. The remaining regions show positive anomaly and are almost statistically insignificant (Figs 2b and c). Similarly, during the CP El Niño, the spatial structure is similar in austral summer and autumn, with the positive anomaly occurring mainly in the central Pacific and southern Australia. The negative anomaly is found in the remaining oceans. Except the Weddell Sea, other areas are statistically insignificant in austral summer and autumn (Figs 2f and g).

In the following austral winter during the years of EP El Niño, the feature of MLD anomaly in the SO exhibits a dipole structure, with positive anomaly (Box 1) over the central and western Pacific (40°–60°S, 160°E–145°W) and negative anomaly (Box 2) over the eastern Pacific (45°–65°S, 140°–70°W). The Indian and Atlantic sectors show a weak and statistically insignificant positive anomaly (Fig. 2d). One can see two negative MLD anomaly centers and one positive anomaly center in austral winter in the CP El Niño cases. Negative anomaly centers occur in the central Pacific and Indian Ocean, while the positive anomaly center occurs in southern Australia. But only the negative anomaly center in the central Pacific (42°–62°S, 165°–100°W) features the strong and statistically significant negative anomaly (Box 3), which is distinct from that of EP El Niño. The above results indicate that both EP and CP El Niño events have dominant impacts on the MLD anomaly in the southern Pacific in austral winter compared with the other three seasons, while the influences are markedly different. We find that the MLD anomaly associated with EP El Niño shows a dipole-like pattern in the Pacific sector during the austral winter (Boxes 1 and 2 in Fig. 2d), while during the CP El Niño, only a separate negative anomaly center (statistically significant) exists in the Pacific sector (Box 3 in Fig. 2h). These response characteristics are different from previous investigations, which indicated that the MLD dipole emerges in spring during EP El Niño. Moreover, they found the MLD dipole located in the Pacific (negative anomaly center) and Atlantic (positive anomaly center) sectors (Wang et al., 2020). Different data sets and study periods, and different methods for defining the EP and CP El Niño and the MLD may all lead to differences in the results. Although the effects of the two types of El Niño on the MLD are significantly different in austral autumn, the impact of CP El Niño on MLD is not statistically significant. In contrast, in austral winter, the effects of two types of El Niño on MLD are statistically significant, which makes comparisons of the different effects valid. On the other hand, austral winter is the deepest season for the MLD, which has a significant impact on both SO primary productivity and global climate change. In addition, although the El Niño during the austral winter is in the decaying phase, the effect on the MLD is strongest at this season. This prompts this study to primarily focus on the different impacts of two types of El Niño events on the MLD of the Pacific sector in austral winter.

4 Tropical teleconnections

Previousnresults have revealed that the two types of El Niño events are accompanied by SSTA at different spots. This section first examines the SSTA triggered by the EP and CP El Niño events in the Pacific sector (Fig. 3), where the austral winter MLD anomaly is most pronounced (Figs 2d and h). During the EP El Niño, the SSTA is most obvious near the equator (Fig. 3a). The positive SSTA occurs in the eastern Pacific south of the equator, extending westward to 180°. The positive SSTA center appears off western Peru, yet the SSTA here is statistically insignificant. The negative SSTA is zonally distributed along the equator with longitudes ranging from 180° to 100°W. It is also not statistically significant. Instead, the statistically significant region appears in the extratropical Pacific between 160°E and 70°W, characterized by a dipole distribution pattern as well. It is noted that the dipole position of SSTA is consistent with that of the MLD dipole (Figs 2d and 3a). The negative SSTA occurs exactly where the ML abnormally deepens (Box 1), while positive SSTA occurs where the ML shoals (Box 2). In addition to the tropical Pacific, a small proportion of significant positive SSTA exists in the northern Indian Ocean near the coast. In comparison, the maximum positive SSTA of CP El Niño emerges in the central Pacific, with 10°–30° of westward shifting compared with the EP El Niño events (Fig. 3b). Although the magnitudes of this positive anomaly are smaller than that of the EP El Niño, they are statistically significant at the

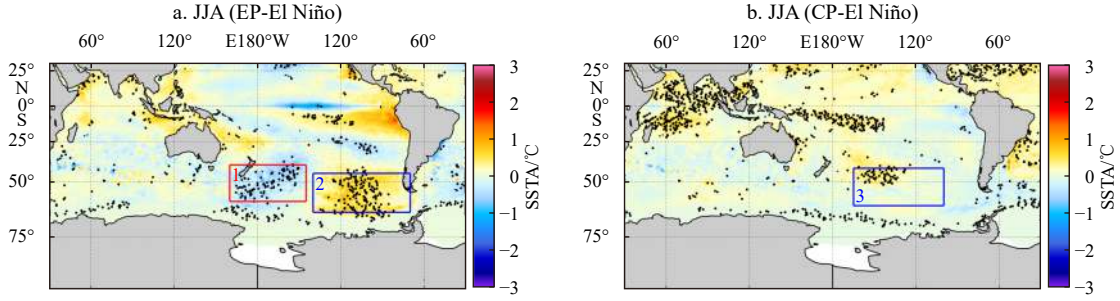

Fig. 3. Composite images of SSTA observed from the ERA5 for EP (a) and CP (b) El Niño events in austral winter (JJA, June, July, and August). The black stippled areas represent that the results are statistically significant at the 95% confidence level. Box 1 (red; 40°–60°S, 160°E–180°–145°W) and Box 2 (blue; 45°–65°S, 140°–70°W) in a and Box 3 (blue; 42°–62°S, 165°–100°W) in b indicate the focus areas, same as Boxes 1, 2, and 3 in Figs 2d and h.

95% confidence level. During the CP El Niño events, the positive SSTA occurs to the northwest of Box 3 and the position of positive SSTA is not completely coincident with Box 3 (Fig. 3b). Additionally, statistically significant positive SSTA is found in almost entire the northern Indian Ocean, which is different from the EP El Niño. The statistically significant SSTA and MLD anomaly are in good agreement, suggesting a possible connection between the two. The mechanisms will be discussed in a later section.

Previous studies have shown that the positive SSTA associated with the El Niño in the tropical Pacific can heat the atmosphere and enhance atmospheric convection (Cai et al., 2011; Clem and Fogt, 2015; Karoly and Hoskins, 1983). It can be regarded as an effective Rossby wave source, which can excite the Rossby wave train propagating poleward in the upper troposphere. Figure 4 shows the austral winter geopotential heights of the upper, middle, and lower troposphere during the EP and CP El Niño events. One can see that in the upper troposphere, the Rossby wave train propagates from the tropical region to the Antarctic region via alternating cyclone anomaly and anticyclone anomaly on the 300 hPa geopotential height anomaly, which is known as the Pacific-South American (PSA) pattern (Figs 4a and b). During the EP El Niño, the 300 hPa geopotential height anomaly extends along an approximate great circle path, originating from the eastern Australia and propagating southeastward into the Southeast Pacific and finally into the Amundsen Sea, characterized by a positive (far east of Australia)-negative (Ross Sea–Amundsen Sea) anomaly centers (Fig. 4a). As a result, low-pressure anomaly center, known as the cyclonic anomaly, dominates the Ross Sea–Amundsen Sea. During the CP El Niño, the Rossby wave train has a similar spatial propagation path to that of EP-Niño, featuring positive (eastern Australia)-negative (southern New Zealand)-positive (Amundsen Sea–Bellingshausen Sea) anomaly centers. In contrast to the EP El Niño, the Amundsen–Bellingshausen seas are controlled by the positive geopotential height anomaly center, namely anticyclonic anomaly (Fig. 4b). Since the interval of geopotential height contours is

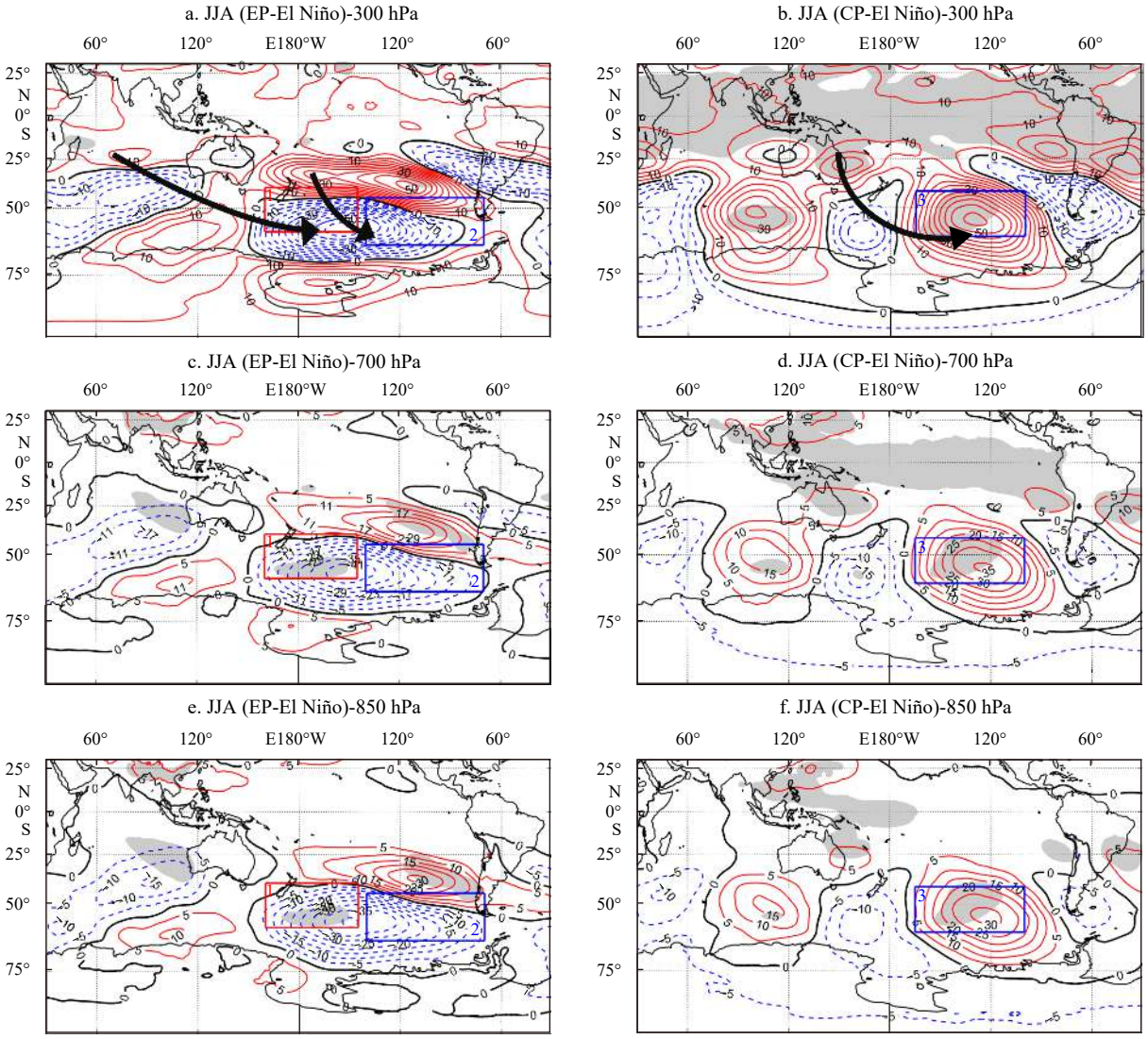

Fig. 4. Composite images of 300 hPa (a and b), 700 hPa (c and d), and 850 hPa (e and f) geopotential height anomaly (unit: m) in austral winter (JJA) derived from the ERA5 for EP El Niño (a, c, and e) and CP El Niño (b, d, and f) events. The gray shadings represent the results statistically significant at the 95% confidence level. Red solid, black solid, and blue dashed lines for geopotential height anomaly indicate the positive, zero, and negative anomalies, respectively. Black arrow indicates the path of Rossby wave propagation. Box 1 (red; 40°–60°S, 160°E–180°–145°W) and Box 2 (blue; 45°–65°S, 140°–70°W) and Box 3 (blue; 42°–62°S, 165°–100°W) in b, d, and f indicate the focus areas, same as Boxes 1, 2, and 3 in Figs 2 d and h.

5 m, the PSA structure of the EP El Niño is stronger than that in the CP El Niño cases. In the middle and lower troposphere, the phenomenon of Rossby wave train propagation is weaker or even disappears, but the Ross Sea–Amundsen Sea and the Amundsen Sea–Bellingshausen Sea are still dominated by a low-pressure anomaly (EP El Niño) and high-pressure anomaly (CP El Niño) centers, respectively (Figs 4c–f). The above analysis results indicate that tropical Pacific warm SSTA with different magnitudes and placements induce different geopotential height anomalies near the Amundsen Sea in terms of intensity and location.

The Rossby wave train only spreads poleward during three seasons rather than summer, when the subtropical jet is sufficiently strong and properly positioned to act as a waveguide (Li et al., 2015b; Schneider et al., 2012). Figure 5 shows the austral winter 300 hPa zonal wind speed anomaly together with the PV anomaly during the two types of El Niño. During the EP El Niño, the subtropical jet (38°–60°S, 160°E–180°–70°W) at the MLD dipole region is substantially stronger than the climatology, ranging from southeast of Australia to west of Chile around 50°S (Fig. 5a). From Fig. 5c, in the meridional direction, the PV anomaly exhibits distinctive positive-negative-positive distribution patterns in the South Pacific. The positive PV anomaly (25°–50°S, 160°E–180°–70°W) occurs between 25°S and the northern dipole pattern, ranging latitudinally from southeastern Australia to western Chile. Negative PV anomaly (40°–65°S, 160°E–180°–70°W) occurs at the dipole pattern, with the negative anomaly center located on the western border of Box 2. Another positive PV anomaly (65°–80°S, 160°E–110°W) exists to the south of the negative PV anomaly. Moreover, positive (25°–50°S, 160°E–180°–70°W) and negative PV anomalies (40°–65°S, 160°E–70°W) appear to the north and south of the subtropical jet (38°–60°S, 160°E–180°–70°W), respectively (Fig. 5c). This exceptionally strong subtropical jet and the meridional PV gradient in its vicinity facilitate the propagation of the Rossby wave train. However, in the case of the CP El Niño, the subtropical jet is not visible and the meridional PV gradient is substituted by the zonal gradient (Figs 5b and d). This illustrates that the intensity of the PSA pattern may also influence the circulation near Amundsen Sea in addition to the different heat sources in the tropical Pacific. Conditions favoring southeastward propagation of Rossby wave trains may result in a stronger PSA pattern.

5 Possible modulation mechanisms

The last section investigates poleward propagation of the El Niño-induced Rossby wave trains in the upper troposphere, thus this section further explores responses of near-surface ocean circulation. Figure 6 shows the SLP anomaly and 10 m wind speed anomaly attributed to the EP and CP El Niño. The positive SSTA associated with the EP El Niño excites a Rossby wave train propagating towards the vicinity of the Amundsen Sea, which intensifies the ASL (Fig. 6a). Consequently, a strong anomalous cyclone formed in the Ross Sea–Amundsen Sea–Bellingshausen Sea. Strong southerly and northerly wind speed anomalies occur to the west and east of the anomalous cyclone, respectively, where the MLD dipole occurs (Figs 2d and 6c). In contrast, the CP El Niño events cause anomalous anticyclone only in the Amundsen Sea–Bellingshausen Sea (Fig. 6b). Remarkable northerly wind speed anomaly occurs to the west of this anomalous anticyclone, precisely where the negative MLD anomaly occurs (Figs 2h and 6d). Despite the cold southerly winds to the east of the anomalous anticyclone, it fails to directly affect the MLD in Box 3, as it is located to the east of Box 3. One can see that the strong anomalous cyclone appears in the MLD dipole region (Boxes 1 and 2) during the EP El Niño, while the strong anomalous anticyclone occurs in the region of negative MLD anomaly (Box 3) during the CP El Niño events, which enhances the lateral transport of the corresponding meridional winds of two flanks. It suggests that the meridional winds associated with anomalous cyclones and anticyclones are critical factors to create distinct effects of two types of El Niño events on the MLD anomaly. In addition, the anomalous cyclone is only observed during the EP El Niño events, which is similar to the response of the SLP anomaly

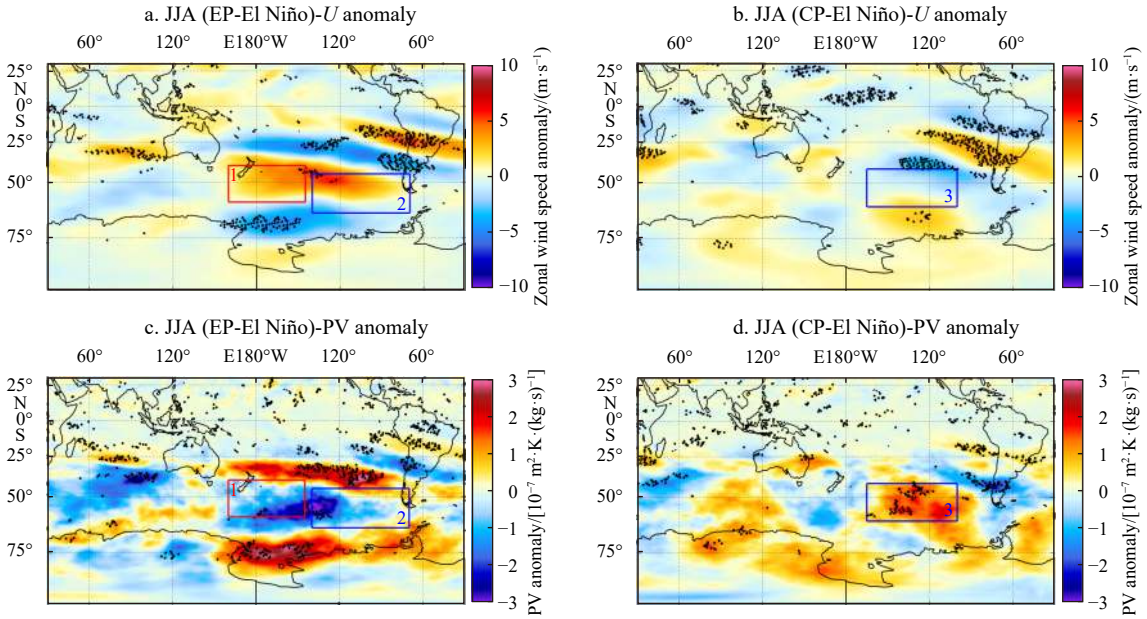

Fig. 5. Composite images of austral winter (JJA, June, July, and August) 300 hPa zonal wind speed anomaly derived from the ERA5 for EP El Niño (a) and CP El Niño (b) events and potential vorticity (PV) anomaly derived from the ERA5 for EP El Niño (c) and CP El Niño (d) events. The black stippled areas represent the results statistically significant at the 95% confidence level. Box 1 (red; 40°–60°S, 160°E–180°–145°W) and Box 2 (blue; 45°–65°S, 140°–70°W) and Box 3 (blue; 42°–62°S, 165°–100°W) indicate the focus areas, same as Boxes 1, 2, and 3 in Figs 2d and h.

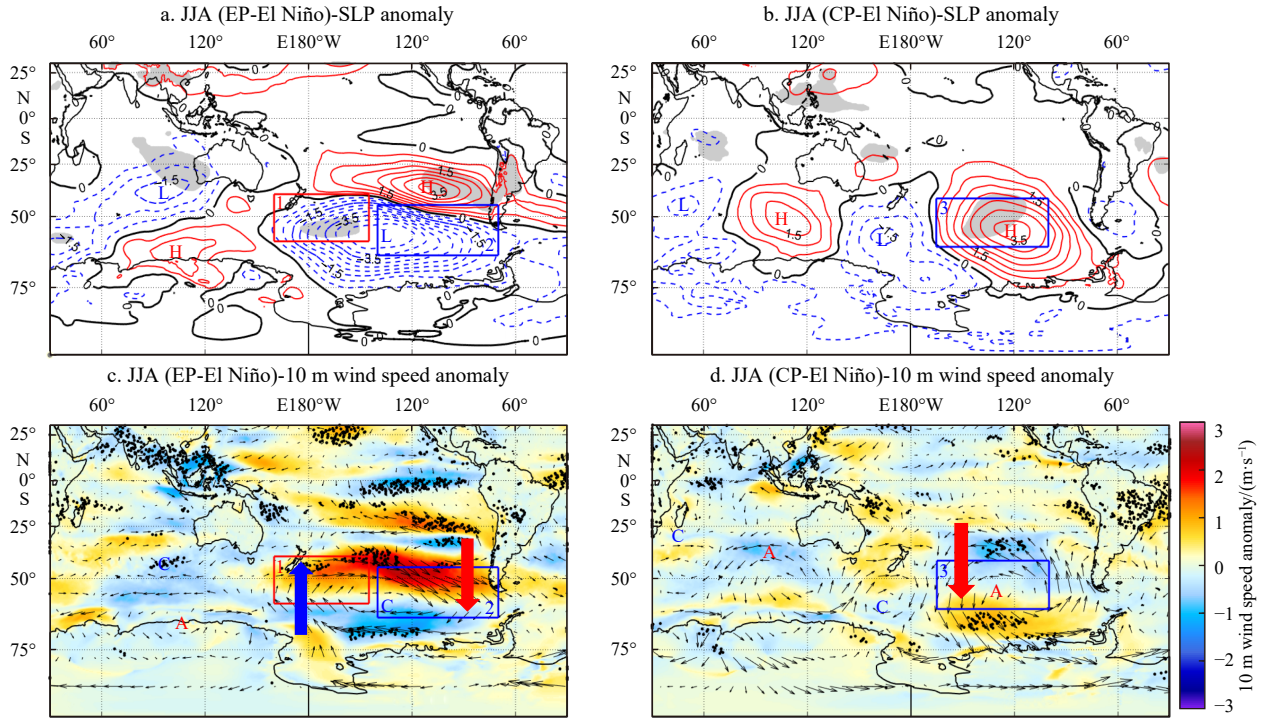

Fig. 6. Composite images of SLP anomaly (a and b, unit: hPa) (contours), and anomalous 10 m wind (c and d) (vectors) as well as wind speed (color) anomaly (unit: m/s) derived from the ERA5 for EP El Niño (a and c) and CP El Niño (b and d) events. Red solid, black solid, and blue dashed lines for SLP anomaly indicate the positive, zero, and negative anomalies, respectively. The gray shadings and black stippled areas represent the results statistically significant at the 95% confidence level. The red letters H and A represent the High-pressure anomaly center and anticyclone, respectively. The blue letters L and C represent the Low-pressure anomaly center and cyclone, respectively. Box 1 (red; 40°–60°S, 160°E–180°–145°W) and Box 2 (blue; 45°–65°S, 140°–70°W) in a and c and Box 3 (blue; 42°–62°S, 165°–100°W) in b and d indicate the focus areas, same as Boxes 1, 2, and 3 in Figs 2d and h.

field to unclassified ENSO (Li and England, 2020). However, the Amundsen Sea is controlled by the anomalous anticyclone in the CP El Niño, which has not been studied yet.

The different sources of meridional winds exhibit different

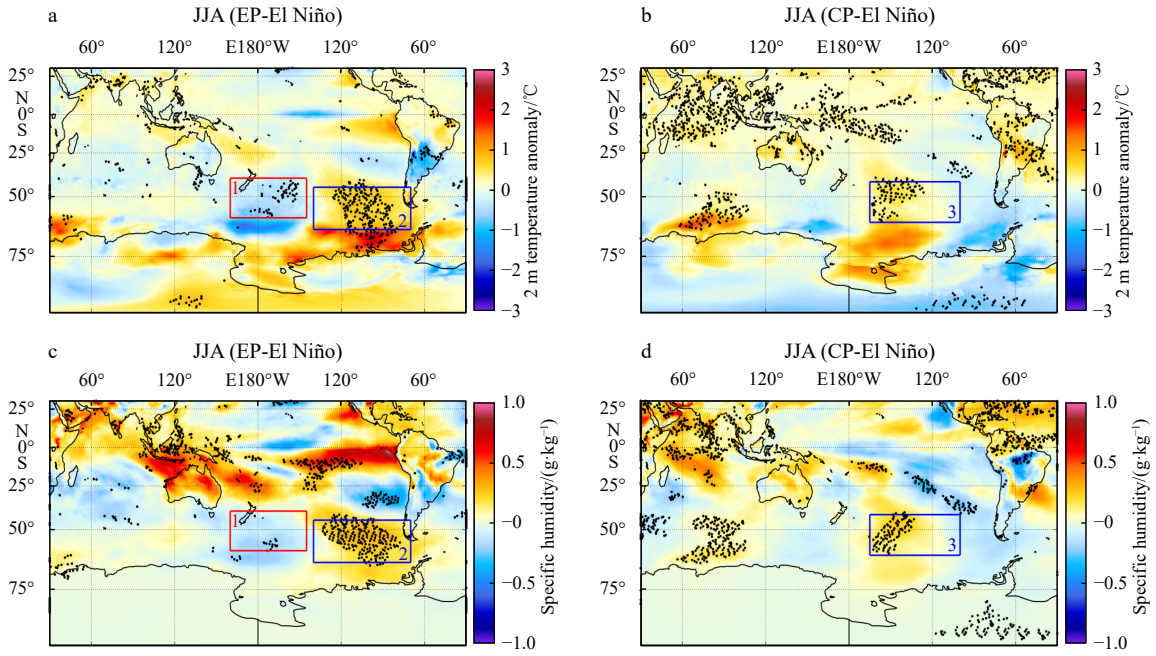

Fig. 7. Composite images of air temperature anomaly at 2 m (a and b), and 1 000 hPa specific humidity anomaly (c and d) derived from the ERA5 for EP El Niño (a and c) and CP El Niño (b and d) events. The black stippled areas represent the results statistically significant at the 95% confidence level. Box 1 (red; 40°–60°S, 160°E–180°–145°W) and Box 2 (blue; 45°–65°S, 140°–70°W) in a and c and Box 3 (blue; 42°–62°S, 165°–100°W) in b and d indicate the focus areas, same as Boxes 1, 2, and 3 in Figs 2d and h.

properties, particularly temperature and humidity. Figure 7 shows temperature anomaly at 2 m and 1 000 hPa specific humidity anomaly in the EP and CP El Niño cases. In the EP El Niño case, the 2 m air temperature anomaly and specific humidity anomaly also show a dipole structure (Figs 7a and c), characterized by colder and drier air appearing in Box 1 (positive MLD anomaly), and warmer and wetter air appearing in the Box 2 (negative MLD anomaly). These are attributed to the anomalous cyclone at the MLD dipole region. During the EP El Niño events, the equatorward winds to the west of the anomalous cyclone deliver colder and drier air to Box 1, whilst poleward winds to the east of the anomalous cyclone advect warmer and wetter air to Box 2 (Fig. 6c). The poleward winds on the west side of the strong anomalous anticyclone transport warmer and wetter air to Box 3 during the CP El Niño, resulting in a warm together with wet anomaly center (Figs 6d, 7b and d).

Furthermore, comparisons of Figs 3a and b to Figs 7a and b show that the distribution of temperature anomaly at 2 m is quite similar to that of the SSTA during the EP and CP El Niño events. However, the fluctuation amplitudes of the SSTA are smaller than that of the 2 m temperature anomaly, implying that the heat exchange exists between the atmosphere and the ocean through sensible heating and then affect the MLD. Therefore, the total heat flux at the air-sea interface is further investigated. Figure 8 shows components of total heat flux anomaly during two types of El Niño. The positive anomaly indicates that the ocean gains the heat from the atmosphere. One can see that during the two types of El Niño, SH and LH anomalies are more pronounced than LW and SW anomalies in the focus regions. During the EP El Niño events, the negative SH anomaly (southeast of New Zealand) and the positive SH anomaly (southwest of Chile) show up in the MLD dipole region (Fig. 8a). In contrast, the negative LH anomaly extends eastward to 100°W compared to the negative SH anomaly (Fig. 8c), which may counteract the warming effect of the positive LH anomaly in Box 2. The LW anomaly is similar to the LH anomaly, but the magnitudes are smaller (Fig. 8e). Comparing to the other three components, the SW anomaly at the MLD dipole region are negligible (Fig. 8g). Accordingly, the spatial distributions of total surface heat flux anomaly are similar to that of the LH anomaly (Figs 8c and i). During the CP El Niño events, except for the SW anomaly, the other three components gain the heat in Box 3 (Figs 8b, d, and f). The SW anomaly here shows a weak and statistically significant negative anomaly with the heat loss (Fig. 8h). The reason for the negative SW anomaly needs to be further explored. Thus, the total surface heat flux anomaly in the CP El Niño cases acquires the heat at the negative MLD anomaly region (Box 3 in Fig. 8j).

These signatures may preliminarily explain the different results of SSTA and MLD anomaly during two types of El Niño events, i.e., the MLD (SSTA) dipole in the EP El Niño cases and separate negative MLD (positive SSTA) anomaly center in the CP El Niño cases. During the EP El Niño events, the ocean loses the heat off the southeastern of New Zealand (Box 1, positive MLD anomaly region), where convection is enhanced and the ML deepens. In contrast, in the southwest of Chile (Box 2, negative MLD anomaly region), the ocean gains the heat from the atmosphere and the ML becomes shallower, even though the heat loss here counteracts the warming effect. As for the CP El Niño events, the ocean acquires the heat from the atmosphere in the central subtropical Pacific (Box 3, negative MLD anomaly region), which enhances stratification and therefore, ML shoals.

Further quantitative analysis of the total surface heat flux anomaly and its components show that during EP El Niño, both the negative surface SH, LH, and SW anomaly contribute to the SST cooling and ML deepening (Box 1), especially the surface SH and LH anomaly (Fig. 9). The regional averaged total heat flux anomaly reaches –4.5 W/m^2, accompanied by SH, LH and SW reaching –1.9 W/m^2, –1.9 W/m^2 and –0.7 W/m^2, respectively. In comparison, the contribution of the total heat flux is negligible in the negative MLD anomaly region (Box 2), characterized by values close to 0, due to the counterbalance of heat gain and loss in this region. During the CP El Niño events (Box 3), the LH reaching 3.6 W/m^2 is the dominant contributor to SST warming and ML shoaling. In addition, the increased SH and LW of 2.7 W/m^2 and 2.6 W/m^2 are two other important contributors to SST warming and ML shoaling. The SW cools the SST with –0.8 W/m^2. Thus, the total heat flux anomaly is 8 W/m^2.

In combination with the surface heat flux anomaly described above, we next examine the austral winter MLD variability driven by surface heat flux anomaly. As shown in Figs 2d and h, the MLD dipole associated with the EP El Niño events occurs in the South Pacific, while only the single negative MLD anomaly center can be found during the CP El Niño events. To comprehensively understand the response of MLD anomaly to El Niño-induced surface heat flux anomaly, the regional means of the three MLD anomaly boxes is shown in Fig. 10. One can see that the MLD increases by 26 m and decreases by 40 m in the MLD dipole region in the EP El Niño cases, while it decreases by 15 m in the CP El Niño cases. It is worth noting that the maximum MLD variation occurs synchronously with the almost zero total heat flux anomaly in EP cases (Box 2 in Figs 9 and 10), suggesting that the surface heat flux is not the primary factor leading to the negative MLD anomaly in Box 2 (southwest of Chile).

The question then arises as to what is responsible for the negative MLD anomaly during the EP El Niño events. The earlier analysis proved that the EP El Niño-related ASL intensifies via the PSA pattern. Subsequently, the enhanced poleward northerly winds to the east of the anomalous cyclone bring warmer air from lower latitudes into the vicinity of the Amundsen Sea. Even though the surface heat flux has no contribution to this negative MLD anomaly in Box 2, the warmer air promotes sea ice melting and facilitates the maintenance of fresh water, which may result in a negative MLD anomaly. To confirm this hypothesis, the SIC anomaly in the EP and CP El Niño cases is shown in Fig. 11. One can see that a strong and statistically significant negative SIC anomaly prevails to the south of Box 2 during the EP El Niño events. Negative SIC anomaly suggests sea ice melting or reduction in sea ice formation, which results in available freshwater on the sea surface. Negative SIC anomaly occurs to the south of Box 2 and does not directly affect MLD change within Box 2. However, this area is dominated by prevailing westerly winds, implying that the northward Ekman transport brings the freshwater from the south into Box 2. As a result, stratification is enhanced and the MLD becomes shallower. In comparison, strong but statistically insignificant positive anomaly and negative SIC anomaly present in the southern Box 1 during the EP El Niño and Box 3 during the CP El Niño, respectively. These suggest that sea ice is a predominant factor in the shallowing of MLD in Box 2, while total surface heat flux anomaly has no effect. Sea ice affects the MLD by varying the strength of stratification. This is inconsistent with previous conclusions, which indicated that the MLD anomaly associated with the EP El Niño is governed by surface heat flux anomaly and wind anomaly (Li and England, 2020; Wang et al., 2020).

6 Discussion and conclusions

In summary, we have shown distinct responses of the austral winter MLD in the SO to the two types of El Niño, i.e., the SO

MLD dipole (Box 1 and Box 2) during the EP El Niño events and the isolated negative MLD anomaly center (Box 3) during the CP El Niño events. The corresponding mechanism is summarized in Fig. 12. Positive SSTA in the central and eastern Pacific associated with the EP El Niño events warm the atmosphere and enhance atmospheric convection, which can act as an effective

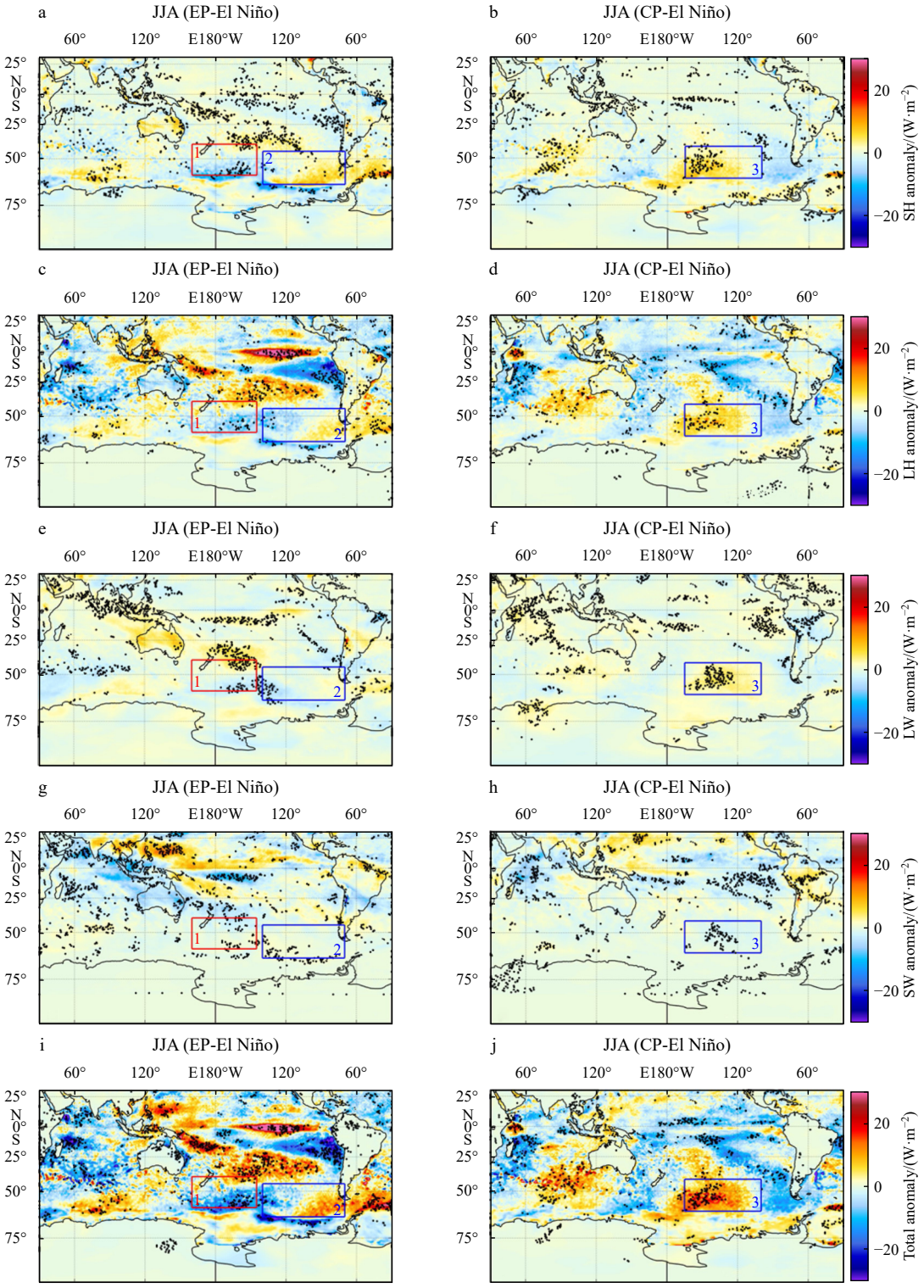

Fig. 8. Composite images of surface sensible heat flux (SH) anomaly (a and b), latent heat flux (LH) anomaly (c and d), net longwave radiation flux (LW) anomaly (e and f), net shortwave radiation flux (SW) anomaly (g and h), and total surface heat flux anomaly (i and j) derived from the ERA5 for EP El Niño (a, c, e, g, and i) and CP El Niño (b, d, f, h, and j) events. The positive anomaly represents downward. The black stippled areas represent the results statistically significant at the 95% confidence level. Box 1 (red; 40°–60°S, 160°E–180°–145°W) and Box 2 (blue; 45°–65°S, 140°–70°W) in a, c, e, g, and i and Box 3 (blue; 42°–62°S, 165°–100°W) in b, d, f, h, and j indicate the focus areas, same as Boxes 1, 2, and 3 in Figs 2d and h.

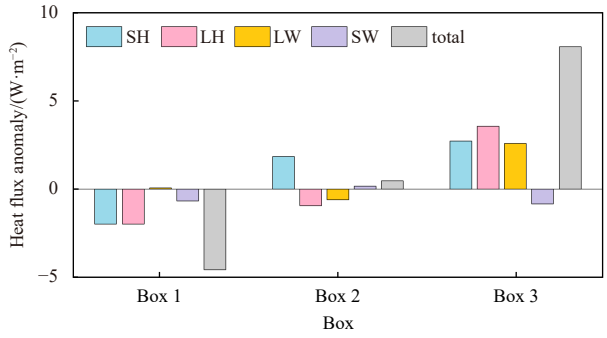

Fig. 9. Contributions of net heat flux components to the MLD anomaly during EP and CP El Niño events. The contributions are calculated from averaged anomaly over Box 1 and Box 2 in Figs 8a, c, e, g, and i for EP El Niño events, and Box 3 in Figs 8b, d, f, h, and j for CP El Niño events.

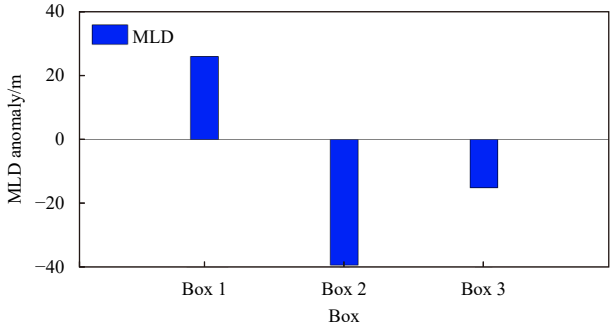

Fig. 10. Magnitudes of MLD variation derived from the ORAS5 during the EP and CP El Niño events. The magnitudes are estimated by averaging anomaly over Boxes 1 and 2 in Fig. 2d and Box 3 in Fig. 2h.

source of the Rossby wave train. The Rossby wave train propagates southeastward along a great circle path in the upper troposphere, ultimately reaching the vicinity of the Amundsen Sea. As a result, the ASL intensifies, enabling the southerly winds to the west of the anomalous cyclone to deliver colder and drier air to the southeast of New Zealand (Box 1). The strong negative air temperature anomaly and weak negative SSTA cause temperature differences at the sea-air interface, resulting in the heat loss on the sea surface, and leading to MLD deepening in Box 1. However, on the other side of the anomalous cyclone, northerly winds transport warmer and wetter air to the southwest of Chile (Box 2). Although the effect of sea surface heat flux is negligible, the warmer air promotes sea ice melting and maintenance of fresh water with subsequent stratification enhancement, thus making MLD shallower in Box 2 (Fig. 12a). During the CP El Niño events, the heat source appears in the central Pacific. The propagation path of the Rossby wave train is similar to that of the EP El Niño, except that the Amundsen Sea is dominated by an anomalous anticyclone. Thus, the poleward winds from the west of the anomalous anticyclone transport warmer and wetter air to the southern Pacific (Box 3). This contributes to warmer air than the ocean. The ocean gains the heat from the atmosphere, thus forming a negative MLD anomaly in Box 3 (Fig. 12b).

From Fig. 10, one can see that the ML variations caused by the EP El Niño events are larger than that of the CP El Niño events. This may be caused by the following three reasons. First, the warm SSTA signal induced by the EP El Niño is stronger than that by the CP El Niño (Fig. 3), which is consistent with the previous results (Kao and Yu, 2009; Ren and Jin, 2011). Therefore, the EP El Niño creates stronger anomalous disturbances in the atmosphere. Second, years of the EP El Niño events coincide with the positive phase of the IOD, and the tropical Indian Ocean also has a Rossby wave train propagating southeastward into the Amundsen Sea (Fig. 4a), resulting in a stronger PSA pattern due to the combined effect of the EP El Niño and the IOD (Zhang et al., 2021). Finally, in the EP El Niño cases, the abnormally strong subtropical jet and the meridional gradient of the PV anomaly are conducive to propagation of the Rossby wave train (Li et al., 2021), which are absent in the CP El Niño cases (Fig. 5).

Based on ORAS5 and ERA5 reanalysis data, we investigate the quite different responses of the MLD to the two types of El Niño. The strongest MLD response to both EP and CP El Niño events occurs in austral winter, accompanied by an EP-induced SO MLD dipole pattern and a separate CP-induced negative MLD anomaly center. The two types of El Niño have different strengths of tropical warm SST anomalous signals. Therefore, the PSA patterns vary in strength, i.e., the southeastward propagation of the Rossby wave train. As a result, the ASL strengthens during the EP El Niño, with an anomalous cyclone dominating the Amundsen Sea, while the ASL weakens during the CP El Niño, with an anomalous anticyclone controlling the Amundsen Sea. During the EP El Niño events, the positive MLD anomaly occurs in the southeast of New Zealand (Box 1, 40°–60°S, 160°E–180°–145°W), while the negative anomaly occurs in the southwest of Chile (Box 2, 45°–65°S, 140°–70°W). The southerly winds to the west of the anomalous cyclone exacerbate the temperature and humidity differences between the air and the sea surface, subsequently causing variations in the surface heat flux. Among the four components of the total surface heat flux, negative SH anomaly and LH anomaly are the main contributors to surface cooling. This makes the MLD deepen. To the east of the anomalous cyclone, the role of sea surface heat fluxes is negligible. However, the warm air from

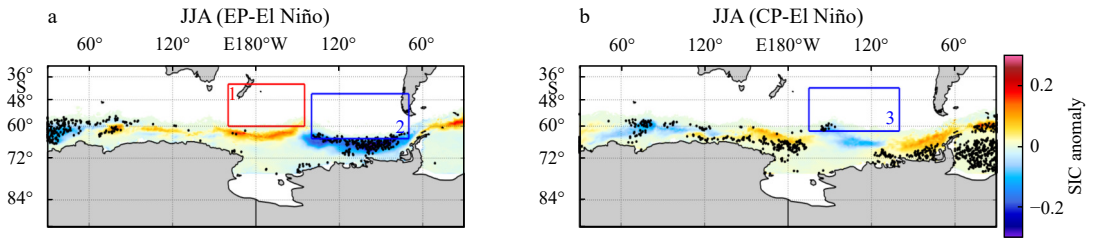

Fig. 11. Composite pictures of SIC anomaly derived from the ORAS5 during EP El Niño events (a) and CP El Niño events (b). The black stippled areas represent the results statistically significant at the 95% confidence level. Box 1 (red; 40°–60°S, 160°E–180°–145°W) and Box 2 (blue; 45°–65°S, 140°–70°W) in a and Box 3 (blue; 42°–62°S, 165°–100°W) in b indicate the focus areas, same as Boxes 1, 2, and 3 in Figs 2d and h.

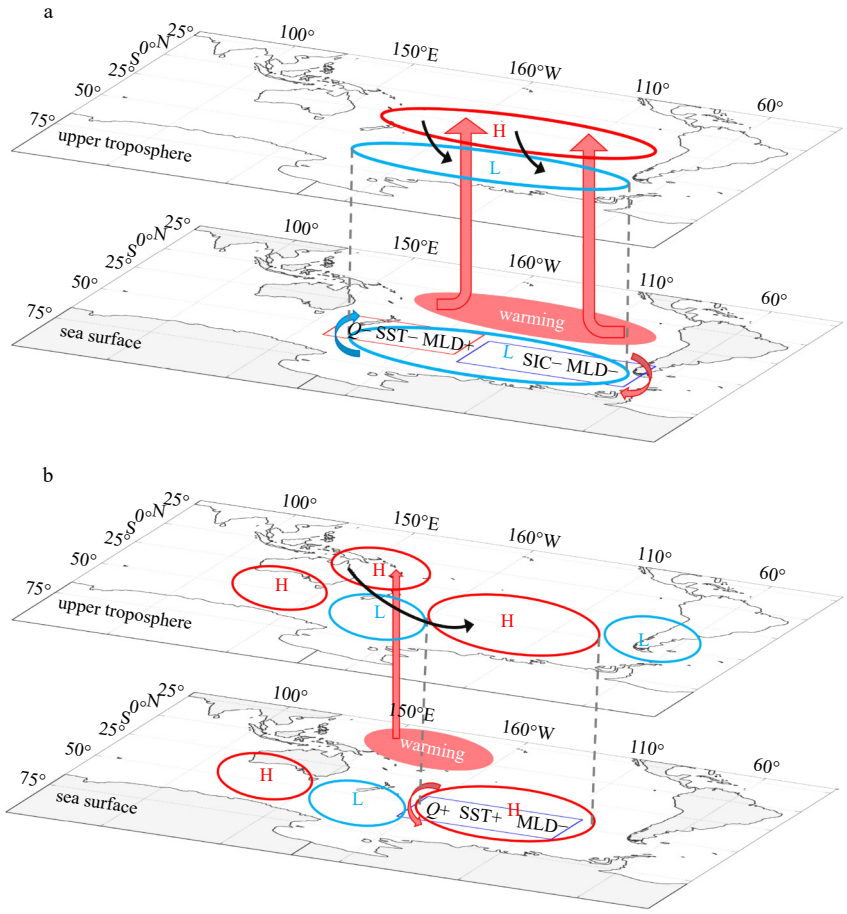

Fig. 12. Schematic diagram illustrating the differences of critical elements during EP and CP El Niño events. Red box (40°–60°S, 160°E–180°–145°W) and blue box (45°–65°S, 140°–70°W) in a and blue box (42°–62°S, 165°–100°W) in b indicate the focus areas, same as Boxes 1, 2, and 3 in Figs 2d and h. Black arrow: Rossby wave train path; pink upward arrow: upward motion; pink and blue curved arrows: wind; H: high-pressure anomaly center; L: low-pressure anomaly center; *Q*: total surface heat flux; +: increase; –: decrease.

the tropics melts the sea ice and maintains fresh water, thus resulting in the shallower MLD. The separate negative MLD anomaly center in the CP El Niño cases occurs in the far southeast of New Zealand (Box 3, 42°–62°S, 165°–100°W). Warmer and wetter air to the west of the anomalous anticyclone is transported to Box 3, increasing the temperature difference between the ocean and the atmosphere here. As a result, the sea surface gains the heat from the atmosphere through the positive SH, LH, and LW anomalies, eventually the MLD shoals.

References

Arrigo K R, van Dijken G, Long M. 2008. Coastal Southern Ocean: A strong anthropogenic CO_2 sink. Geophysical Research Letters, 35(21): L21602, doi: 10.1029/2008gl035624

Bell B, Hersbach H, Simmons A, et al. 2021. The ERA5 global reanalysis: preliminary extension to 1950. Quarterly Journal of the Royal Meteorological Society, 147(741): 4186–4227, doi: 10.1002/qj.4174

Bosc C, Delcroix T, Maes C. 2009. Barrier layer variability in the western Pacific warm pool from 2000 to 2007. Journal of Geophysical Research, 114(C6): C06023, doi: 10.1029/2008jc005187

Cai Wenju, Santoso A, Wang Guojian, et al. 2014. Increased frequency of extreme Indian Ocean Dipole events due to greenhouse warming. Nature, 510(7504): 254–258, doi: 10.1038/nature13327

Cai Wenju, van Rensch P, Cowan T, et al. 2011. Teleconnection pathways of ENSO and the IOD and the mechanisms for impacts on Australian rainfall. Journal of Climate, 24(15): 3910–3923, doi: 10.1175/2011jcli4129.1

Cai Wenju, Wu Lixin, Lengaigne M, et al. 2019. Pantropical climate interactions. Science, 363(6430): eaav4236, doi: 10.1126/science.aav4236

Carton J A, Grodsky S A, Liu Hailong. 2008. Variability of the oceanic mixed layer, 1960–2004. Journal of Climate, 21(5): 1029–1047, doi: 10.1175/2007jcli1798.1

Chen Mingcheng, Li T, Wang Xiaohui. 2019. Asymmetry of atmospheric responses to two-type El Niño and La Niña over northwest Pacific. Journal of Meteorological Research, 33(5): 826–836, doi: 10.1007/s13351-019-9022-0

Ciasto L M, England M H. 2011. Observed ENSO teleconnections to Southern Ocean SST anomalies diagnosed from a surface mixed layer heat budget. Geophysical Research Letters, 38(9): L09701, doi: 10.1029/2011gl046895

Clem K R, Fogt R L. 2015. South Pacific circulation changes and their connection to the tropics and regional Antarctic warming in austral spring, 1979–2012. Journal of Geophysical Research: Atmospheres, 120(7): 2773–2792, doi: 10.1002/2014jd022940

de Boyer Montégut C, Madec G, Fischer A S, et al. 2004. Mixed layer depth over the global ocean: an examination of profile data and a profile-based climatology. Journal of Geophysical Research: Oceans, 109(C12): C12003, doi: 10.1029/2004jc002378

de Boyer Montégut C, Mignot J, Lazar A, et al. 2007. Control of salinity on the mixed layer depth in the world ocean: 1. General description. Journal of Geophysical Research: Oceans, 112(C6): C06010, doi: 10.1029/2006jc003953

Ding Qinghua, Steig E J, Battisti D S, et al. 2011. Winter warming in West Antarctica caused by central tropical Pacific warming.

Nature Geoscience, 4(6): 398–403, doi: 10.1038/ngeo1129
Dong Shenfu, Gille S T, Sprintall J. 2007. An assessment of the Southern Ocean mixed layer heat budget. Journal of Climate, 20(17): 4425–4442, doi: 10.1175/jcli4259.1
Dong Shenfu, Sprintall J, Gille S T, et al. 2008. Southern Ocean mixed-layer depth from Argo float profiles. Journal of Geophysical Research: Oceans, 113(C6): C06013, doi: 10.1029/2006jc004051
Duan Rui, Yang Kunde, Ma Yuanliang, et al. 2012. A study of the mixed layer of the South China Sea based on the multiple linear regression. Acta Oceanologica Sinica, 31(6): 19–31, doi: 10.1007/s13131-012-0250-8
Fogt R L, Bromwich D H, Hines K M. 2011. Understanding the SAM influence on the South Pacific ENSO teleconnection. Climate Dynamics, 36(7/8): 1555–1576, doi: 10.1007/s00382-010-0905-0
Foltz G R, McPhaden M J. 2009. Impact of barrier layer thickness on SST in the central tropical North Atlantic. Journal of Climate, 22(2): 285–299, doi: 10.1175/2008jcli2308.1
Gupta A S, England M H. 2006. Coupled ocean-atmosphere-ice response to variations in the southern annular mode. Journal of Climate, 19(18): 4457–4486, doi: 10.1175/JCLI3843.1
Helber R W, Kara A B, Richman J G, et al. 2012. Temperature versus salinity gradients below the ocean mixed layer. Journal of Geophysical Research: Oceans, 117(C5): C05006, doi: 10.1029/2011jc007382
Hersbach H, Bell B, Berrisford P, et al. 2020. The ERA5 global reanalysis. Quarterly Journal of the Royal Meteorological Society, 146(730): 1999–2049, doi: 10.1002/qj.3803
Holte J, Talley L. 2009. A new algorithm for finding mixed layer depths with applications to Argo Data and Subantarctic Mode Water Formation. Journal of Atmospheric and Oceanic Technology, 26(9): 1920–1939, doi: 10.1175/2009jtecho543.1
Hoskins B J, Karoly D J. 1981. The steady linear response of a spherical atmosphere to thermal and orographic forcing. Journal of the Atmospheric Sciences, 38(6): 1179–1196, doi: 10.1175/1520-0469(1981)038<1179:TSLROA>2.0.CO;2
Kao H Y, Yu Jinyi. 2009. Contrasting eastern-Pacific and central-Pacific types of ENSO. Journal of Climate, 22(3): 615–632, doi: 10.1175/2008jcli2309.1
Kara A B, Rochford P A, Hurlburt H E. 2003. Mixed layer depth variability over the global ocean. Journal of Geophysical Research: Oceans, 108(C3): 3079, doi: 10.1029/2000jc000736
Karoly D J, Hoskins B J. 1983. The steady, linear response of the stratosphere to tropospheric forcing. Quarterly Journal of the Royal Meteorological Society, 109(461): 455–478, doi: 10.1002/qj.49710946103
Kidson J W. 1999. Principal modes of Southern Hemisphere low-frequency variability obtained from NCEP-NCAR reanalyses. Journal of Climate, 12(2): 2808–2830, doi: 10.1175/1520-0442(1999)012<2808:PMOSHL>2.0.CO;2
Kug J S, Jin Feifei, An S I. 2009. Two types of El Niño events: cold tongue El Niño and warm pool El Niño. Journal of Climate, 22(6): 1499–1515, doi: 10.1175/2008jcli2624.1
Kuhlbrodt T, Griesel A, Montoya M, et al. 2007. On the driving processes of the Atlantic meridional overturning circulation. Reviews of Geophysics, 45(2): RG2001, doi: 10.1029/2004rg000166
L'Heureux M L, Thompson D W J. 2006. Observed relationships between the El Niño-Southern Oscillation and the extratropical zonal-mean circulation. Journal of Climate, 19(2): 276–287, doi: 10.1175/JCLI3617.1
Li Xichen, Cai Wenju, Meehl G A, et al. 2021. Tropical teleconnection impacts on Antarctic climate changes. Nature Reviews Earth & Environment, 2(10): 680–698, doi: 10.1038/s43017-021-00204-5
Li Qian, England M H. 2020. Tropical Indo-Pacific teleconnections to Southern Ocean mixed layer variability. Geophysical Research Letters, 47(15): e2020GL088466, doi: 10.1029/2020gl088466
Li Xichen, Gerber E P, Holland D M, et al. 2015a. A Rossby wave bridge from the tropical atlantic to west Antarctica. Journal of Climate, 28(6): 2256–2273, doi: 10.1175/jcli-d-14-00450.1
Li Xichen, Holland D M, Gerber E P, et al. 2014a. Impacts of the north and tropical Atlantic Ocean on the Antarctic Peninsula and sea ice. Nature, 505(7484): 538–542, doi: 10.1038/nature12945
Li Xichen, Holland D M, Gerber E P, et al. 2015b. Rossby waves mediate impacts of tropical oceans on west Antarctic Atmospheric Circulation in austral winter. Journal of Climate, 28(20): 8151–8164, doi: 10.1175/jcli-d-15-0113.1
Li Qian, Lee S, England M H, et al. 2019. Seasonal-to-interannual response of Southern Ocean mixed layer depth to the Southern Annular Mode from a global 1/10° ocean model. Journal of Climate, 32(18): 6177–6195, doi: 10.1175/jcli-d-19-0159.1
Li Gang, Li Chongyin, Tan Yanke, et al. 2014b. Observed relationship of boreal winter South Pacific Tripole SSTA with Eastern China rainfall during the following boreal spring. Journal of Climate, 27(21): 8094–8106, doi: 10.1175/jcli-d-14-00074.1
Liu Hailong, Grodsky S A, Carton J A. 2009. Observed subseasonal variability of oceanic barrier and compensated layers. Journal of Climate, 22(22): 6104–6119, doi: 10.1175/2009jcli2974.1
Luo Jingjia, Zhang Ruochao, Behera S K, et al. 2010. Interaction between El Niño and extreme Indian Ocean Dipole. Journal of Climate, 23(3): 726–742, doi: 10.1175/2009jcli3104.1
Meehl G A, Arblaster J M, Bitz C M, et al. 2016. Antarctic sea-ice expansion between 2000 and 2014 driven by tropical Pacific decadal climate variability. Nature Geoscience, 9(8): 590–595, doi: 10.1038/ngeo2751
Mitchell B G, Brody E A, Holm-Hansen O, et al. 1991. Light limitation of phytoplankton biomass and macronutrient utilization in the Southern Ocean. Limnology and Oceanography, 36(8): 1662–1677, doi: 10.4319/lo.1991.36.8.1662
Mo K C, Ghil M. 1987. Statistics and dynamics of persistent anomalies. Journal of the Atmospheric Sciences, 44(5): 877–902, doi: 10.1175/1520-0469(1987)044<0877:SADOPA>2.0.CO;2
Mo K C, Higgins R W. 1998. The Pacific-South American modes and tropical convection during the Southern Hemisphere winter. Monthly Weather Review, 126(6): 1581–1596, doi: 10.1175/1520-0493(1998)126<1581:TPSAMA>2.0.CO;2
Nardelli B B, Guinehut S, Verbrugge N, et al. 2017. Southern Ocean mixed-layer seasonal and interannual variations from combined satellite and in situ data. Journal of Geophysical Research: Oceans, 122(12): 10042–10060, doi: 10.1002/2017jc013314
Nuncio M, Yuan Xiaojun. 2015. The influence of the Indian Ocean Dipole on Antarctic sea ice. Journal of Climate, 28(7): 2682–2690, doi: 10.1175/jcli-d-14-00390.1
Park J, Oh I S, Kim H C, et al. 2010. Variability of SeaWiFs chlorophyll-*a* in the southwest Atlantic sector of the Southern Ocean: strong topographic effects and weak seasonality. Deep-Sea Research Part I: Oceanographic Research Papers, 57(4): 604–620, doi: 10.1016/j.dsr.2010.01.004
Rayner N A, Parker D E, Horton E B, et al. 2003. Global analyses of sea surface temperature, sea ice, and night marine air temperature since the late nineteenth century. Journal of Geophysical Research: Atmospheres, 108(D14): 4407, doi: 10.1029/2002jd002670
Ren Hongli, Jin Feifei. 2011. Niño indices for two types of ENSO. Geophysical Research Letters, 38(4): L04704, doi: 10.1029/2010gl046031
Rondanelli R, Hatchett B, Rutllant J, et al. 2019. Strongest MJO on record triggers extreme Atacama rainfall and warmth in Antarctica. Geophysical Research Letters, 46(6): 3482–3491, doi: 10.1029/2018gl081475
Saji N H, Ambrizzi T, Ferraz S E T. 2005. Indian Ocean Dipole mode events and austral surface air temperature anomalies. Dynamics of Atmospheres and Oceans, 39(1/2): 87–101, doi: 10.1016/j.dynatmoce.2004.10.015
Sallée J B, Speer K G, Rintoul S R. 2010. Zonally asymmetric response of the Southern Ocean mixed-layer depth to the Southern Annular Mode. Nature Geoscience, 3(4): 273–279, doi: 10.1038/ngeo812
Sarmiento J L, Hughes T M C, Stouffer R J, et al. 1998. Simulated response of the ocean carbon cycle to anthropogenic climate

warming. Nature, 393(6682): 245–249, doi: 10.1038/30455
Schneider D P, Okumura Y, Deser C. 2012. Observed antarctic interannual climate variability and tropical linkages. Journal of Climate, 25(12): 4048–4066, doi: 10.1175/jcli-d-11-00273.1
Turner J. 2004. The El Niño-southern oscillation and Antarctica. International Journal of Climatology, 24(1): 1–31, doi: 10.1002/joc.965
Vivier F, Iudicone D, Busdraghi F, et al. 2010. Dynamics of sea-surface temperature anomalies in the Southern Ocean diagnosed from a 2D mixed-layer model. Climate Dynamics, 34(2/3): 153–184, doi: 10.1007/s00382-009-0724-3
Wang Lu, Li T, Chen Lin, et al. 2018a. Modulation of the MJO intensity over the equatorial western Pacific by two types of El Niño. Climate Dynamics, 51(1/2): 687–700, doi: 10.1007/s00382-017-3949-6
Wang Ziqi, Zhang Wenjun, Geng Xin. 2017. Different influences of two types of ENSO on winter temperature and cold extremes in northern China. Acta Meteorologica Sinica (in Chinese), 75(4): 564–580, doi: 10.11676/qxxb2017.038
Wang Zhongpeng, Zhang Zhaoru, Zhou Meng, et al. 2020. Seasonal linkage of the Southern Hemisphere extratropical climate variability to two types of ENSO. Acta Oceanologica Sinica, 39(1): 63–73, doi: 10.1007/s13131-019-1528-x
Xiao Xianjun, Wang Dongxiao, Zhou Wen, et al. 2013. Impacts of a wind stress and a buoyancy flux on the seasonal variation of mixing layer depth in the South China Sea. Acta Oceanologica Sinica, 32(9): 30–37, doi: 10.1007/s13131-013-0349-6
Yeh S W, Kug J S, Dewitte B, et al. 2009. El Niño in a changing climate. Nature, 461(7263): 511–514, doi: 10.1038/nature08316
Ying Meijia, Liu Hailong, Wang Fuchang, et al. 2019. Spatio-temporal variations of mixed layer depth in Southern Ocean. Oceanologia et Limnologia Sinica (in Chinese), 50(6): 1223–1232, doi: 10.11693/hyhz20190800153
Yu Jinyi, Kao H Y. 2007. Decadal changes of ENSO persistence barrier in SST and ocean heat content indices: 1958–2001. Journal of Geophysical Research: Atmospheres, 112(D13): D13106, doi: 10.1029/2006jd007654
Zhang Wenjun, Jin Feifei, Li Jianping, et al. 2011. Contrasting impacts of two-type El Niño over the western North Pacific during boreal autumn. Journal of the Meteorological Society of Japan. Ser. II, 89(5): 563–569, doi: 10.2151/jmsj.2011-510
Zhang Chao, Li T, Li Shuanglin. 2021. Impacts of CP and EP El Niño events on the Antarctic sea ice in austral spring. Journal of Climate, 34(23): 9327–9348, doi: 10.1175/jcli-d-21-0002.1
Zhang Wenjun, Mei Xuebin, Geng Xin, et al. 2019. A nonstationary ENSO-NAO relationship due to AMO modulation. Journal of Climate, 32(1): 33–43, doi: 10.1175/jcli-d-18-0365.1
Zhang Zhaoru, Uotila P, Stössel A, et al. 2018. Seasonal southern hemisphere multi-variable reflection of the southern annular mode in atmosphere and ocean reanalyses. Climate Dynamics, 50(3/4): 1451–1470, doi: 10.1007/s00382-017-3698-6
Zuo Hao, Balmaseda M A, Tietsche S, et al. 2019. The ECMWF operational ensemble reanalysis-analysis system for ocean and sea ice: a description of the system and assessment. Ocean Science, 15(3): 779–808, doi: 10.5194/os-15-779-2019